

# A search for a fifth planet around HR 8799 using the star-hopping RDI technique at VLT/SPHERE<sup>★</sup>

Z. Wahhaj<sup>1,5</sup>, J. Milli<sup>1,2</sup>, C. Romero<sup>1,2</sup>, L. Cieza<sup>3,4</sup>, A. Zurlo<sup>3,4,5</sup>, A. Vigan<sup>5</sup>, E. Peña<sup>1</sup>, G. Valdes<sup>1</sup>, F. Cantalloube<sup>6</sup>, J. Girard<sup>7</sup>, and B. Pantoja<sup>8</sup>

<sup>1</sup> European Southern Observatory, Alonso de Córdova 3107, Vitacura Casilla 19001, Santiago, Chile  
e-mail: [zwahhaj@eso.org](mailto:zwahhaj@eso.org)

<sup>2</sup> Université Grenoble Alpes, CNRS, IPAG, 38000 Grenoble, France

<sup>3</sup> Núcleo de Astronomía, Facultad de Ingeniería y Ciencias, Universidad Diego Portales, Av. Ejercito 441, Santiago, Chile

<sup>4</sup> Escuela de Ingeniería Industrial, Facultad de Ingeniería y Ciencias, Universidad Diego Portales, Av. Ejercito 441, Santiago, Chile

<sup>5</sup> Aix Marseille Univ, CNRS, CNES, LAM, Marseille, France

<sup>6</sup> Max Planck Institute for Astronomy, Königstuhl 17, 69117 Heidelberg, Germany

<sup>7</sup> Space Telescope Science Institute, 3700 San Martin Dr., Baltimore, MD 21218, USA

<sup>8</sup> Department of Physics and Astronomy, Bucknell University, Lewisburg, PA 17837, USA

Received 30 June 2020 / Accepted 21 December 2020

## ABSTRACT

**Context.** Direct imaging of extrasolar giant planets demands the highest possible contrasts ( $\Delta H \gtrsim 10$  mag) at the smallest angular separations ( $\sim 0.1''$ ) from the star. We present an adaptive optics observing method, called star-hopping, recently offered as standard queue observing (service mode) for the SPHERE instrument at the VLT. The method uses reference difference imaging (RDI) but, unlike earlier RDI applications, images of a reference star for PSF subtraction are obtained within minutes of observing the target star.

**Aims.** We aim to significantly gain in contrast beyond the conventional angular differencing imaging (ADI) method to search for a fifth planet at separations less than 10 au, interior to the four giant planets of the HR 8799 system. The most likely semimajor axes allowed for this hypothetical planet, which were estimated via dynamical simulations in earlier works, were 7.5 au and 9.7 au within a mass range of  $1-8 M_{\text{Jup}}$ .

**Methods.** We obtained 4.5 h of simultaneous low-resolution integral field spectroscopy ( $R \sim 30$ ,  $Y-H$  band with IFS) and dual-band imaging ( $K1$  and  $K2$  bands with IRDIS) of the HR 8799 system, interspersed with observations of a reference star. The reference star was observed for about one-third of the total time and generally needs to be of similar brightness ( $\Delta R \lesssim 1$  mag) and separated on sky by  $\lesssim 1-2^\circ$ . The hops between stars were made every 6–10 min, with only 1 min gaps in on-sky integration per hop.

**Results.** We did not detect the hypothetical fifth planet at the most plausible separations, 7.5 and 9.7 au, down to mass limits of  $3.6 M_{\text{Jup}}$  and  $2.8 M_{\text{Jup}}$ , respectively, but attained an unprecedented contrast limit of 11.2 magnitudes at  $0.1''$ . We detected all four planets with high signal-to-noise ratios. The  $YJH$  spectra for planets  $c$ ,  $d$  were detected with redder  $H$ -band spectral slopes than found in earlier studies. As noted in previous works, the planet spectra are matched very closely by some red field dwarfs. Finally, comparing the current locations of the planets to orbital solutions, we found that planets  $e$  and  $c$  are most consistent with coplanar and resonant orbits. We also demonstrated that with star-hopping RDI, the contrast improvement at  $0.1''$  separation can be up to 2 mag.

**Conclusions.** Since ADI, meridian transit and the concomitant sky rotation are not needed, the time of observation can be chosen from within a window that is two to three times larger. In general, star-hopping can be used for stars fainter than  $R = 4$  magnitudes, since for these a reference star of suitable brightness and separation is usually available.

**Key words.** planets and satellites: detection – planets and satellites: atmospheres – instrumentation: adaptive optics – techniques: high angular resolution – techniques: imaging spectroscopy – methods: observational

## 1. Introduction

Radial velocity (RV) surveys have revealed to us the exoplanet population orbiting within  $\sim 5$  au of their parent stars (Mayor et al. 2011; Fernandes et al. 2019). Transit techniques have done the same for the population of closer-in planets ( $\lesssim 1$  au), providing us a glimpse of their atmospheres as inferred from their spectra (Howard et al. 2010; Dong & Zhu 2013; Madhusudhan 2019). Direct imaging on the other hand has found more than a dozen planets orbiting farther than 10 au from their stars<sup>1</sup>. Direct

imaging and interferometry are the only methods that allow us to obtain spectra of exoplanets separated by more than a few astronomical units from their host stars (Bonnetfoy et al. 2014, 2016). Direct imaging is also the only technique that captures protoplanetary disks in the act of forming planets (Keppler et al. 2018; Müller et al. 2018; Haffert et al. 2019). Moreover, it has shown us fully formed planetary systems with their leftover dusty planetesimal disks (Lagrange et al. 2012) and has captured these dust-producing rocky disks at various stages over their lifetime (e.g., Boccaletti et al. 2018, 2020; Wahhaj et al. 2016).

Studies of systems like HR 8799 with its four planets, can offer us a glimpse at possible early (age  $< 30$  Myr) architectures (Marois et al. 2010), perhaps at a stage prior to major planet

<sup>★</sup> The reduction software used in this paper has been made available online (<https://github.com/zwahhaj/starhopping>).

<sup>1</sup> <http://exoplanet.eu/>

migration and scattering (Chatterjee et al. 2008; Crida et al. 2009; Raymond et al. 2010). However, the extrasolar Jupiter and Saturn analogs are mostly still hidden from us, orbiting in the glare of their parent stars between 5 au and 10 au (Fernandes et al. 2019). Fortunately, a giant planet at an age of 30 Myr can be a hundred times brighter than at 300 Myr (e.g., Allard et al. 2012a). With direct imaging, we are trying to detect the younger component of this hidden population, bridging the unexplored gap to connect to the RV and transit exoplanet populations closer in. In fact, some of the deepest direct imaging surveys have nearly completed and yielded a few more giant planets that are fainter and orbiting closer to their stars than in earlier surveys, but mostly these surveys report that the regions beyond 10 au rarely have planets more massive than  $3\text{--}5 M_{\text{Jup}}$  (Nielsen et al. 2019; Chauvin et al. 2017; Macintosh et al. 2015).

The success of the direct imaging technique, especially for ground-based instruments, imaging dozens of exoplanets and protoplanetary disks has been mainly due to angular and spectral difference imaging (ADI, SDI, and ASDI; Liu 2004; Marois et al. 2006; Sparks & Ford 2002; Wahhaj et al. 2011). Without point spread function (PSF) differencing, within minutes we hit a wall in terms of sensitivity because of quasi-static speckles in adaptive optics (AO) images. Speckles essentially mimic astronomical point sources, integrating more like signal than noise. The ADI, SDI and other related techniques decouple the speckles from the real signal, allowing them to be isolated and subtracted. However, these techniques are hampered by the self-subtraction problem (Marois et al. 2006). Since the decoupling of speckles and astronomical signal is never complete, there is inevitably some self-subtraction of signal. This can be manageable for planets moderately separated from the star, where we just lose sensitivity depending on the subtraction algorithm used (e.g., Wahhaj et al. 2013, 2015). However, for planet-star separations of one to two resolution elements and extended structures such as circumstellar disks, the signal can be completely subtracted or the morphology can be significantly altered or completely masked (Milli et al. 2012).

Reference difference imaging (RDI), a possible solution, has been routinely used in space telescope observations (e.g., Weinberger et al. 1999; Choquet et al. 2016), as the PSF is quite stable over successive orbits of the telescope. However, RDI is not often used in ground-based observing where PSFs change significantly over hours. This is because prior to extreme AO the PSF of other stars could not closely match the target PSFs in speckle similarity, especially if the reference star images were not obtained the same night as the science target. Nevertheless, impressive ground-based results on quite a few targets have been achieved (Lagrange et al. 2009; Xuan et al. 2018; Ruane et al. 2019; Bohn et al. 2020). In the more recent efforts, reference PSFs were obtained 30 min to hours apart and the telescope operator would have to manually set up the guiding for each target change, costing significant human effort and photon dead time. Starting recently at the Very Large Telescope, on the SPHERE instrument (VLT/SPHERE), we now offer fast automated RDI available in queue mode for the first time, requiring only a one minute gap for each target change, a technique called star-hopping RDI. To demonstrate the power of this new observing mode and to look for new planets closer to the star, we targeted HR 8799, the home of the four giants.

HR 8799 is a young main-sequence star (age 20–160 Myr; Cowley et al. 1969; Moór et al. 2006; Marois et al. 2008; Hinz et al. 2010; Zuckerman et al. 2011; Baines et al. 2012) at a distance of  $41.29 \pm 0.15$  pc (Gaia Collaboration 2018). The space

motions of the star suggest membership in the Columbia moving group (age 30–40 Myr; Torres et al. 2008; Zuckerman et al. 2011; Bell et al. 2015; Geiler et al. 2019). It has four directly imaged giant planets at projected distances of 15, 27, 43, and 68 au (Marois et al. 2008, 2010). The upper limit to the masses from orbital stability requirements and the derived luminosities assuming an age of  $\sim 30$  Myr suggest that the planet masses are  $5\text{--}7 M_{\text{Jup}}$  (Marois et al. 2010; Currie et al. 2011; Sudol & Haghhighipour 2012). Interior and exterior to the planets, warm dust at 6–10 au and an exo-Kuiper belt beyond 100 au have been detected (Sadakane & Nishida 1986; Su et al. 2009; Hughes et al. 2011; Matthews et al. 2014; Booth et al. 2016). Thus, it is likely that the planets formed in a circumstellar disk, instead of directly from a protostellar cloud as in binary or multiple star formation. However, it is currently a theoretical challenge to form so many massive planets in a single system.

The total system architecture and stability, considering the age, mass, and debris disk formation history have been studied in some detail (see Goździewski & Migaszewski 2009, 2014, 2018; Reidemeister et al. 2009; Su et al. 2009; Fabrycky & Murray-Clay 2010; Moro-Martín et al. 2010; Galicher et al. 2011; Marleau & Cumming 2014; Matthews et al. 2013; Booth et al. 2016; Konopacky et al. 2016; Wilner et al. 2018; Geiler et al. 2019). HR 8799 is a star of the  $\lambda$  Bootis type (indicating an iron poor atmosphere) and also a  $\gamma$  Dor variable, indicating small surface pulsations perhaps also due to some accretion-associated chemical peculiarity (Saio et al. 2018; Saio 2019; Takata et al. 2020). Spectra of the planets has been obtained in the NIR bands with Keck/OSIRIS (Barman et al. 2011, 2015; Konopacky et al. 2013), Project 1640 at Palomar (Oppenheimer et al. 2013), VLT/NACO (Janson et al. 2010), GPI (Ingraham et al. 2014), and SPHERE (Zurlo et al. 2016; Bonnefoy et al. 2016). The comparison of the spectra to brown dwarfs, cool field objects, and current atmospheric models suggest patchy thin and thick clouds of uncertain height, non-equilibrium chemistry, and a dusty low-gravity atmosphere (Marois et al. 2008; Currie et al. 2011; Madhusudhan et al. 2011; Skemer et al. 2012; Marley et al. 2012; Morley et al. 2012; Apai et al. 2013; Buenzli et al. 2015). Given the theoretical challenge in explaining such a massive multi-planet and debris disk system with detailed and specific information, and the prospect of finding additional planets (Goździewski & Migaszewski 2014, 2018) the system deserves a deeper look. We describe our SPHERE study of HR 8799 in the following sections. The reduction software used in this paper can be found online<sup>2</sup>.

## 2. Observations

### 2.1. Telescope and instrument control for star-hopping

The goal of star-hopping on VLT/SPHERE is to switch from recording AO corrected images of the science star to recording those of the reference star with only roughly a one minute gap. Thus the usual help from the human operator to set up the guide star for the active optics correction of the primary mirror, typically a five-minute interaction, should be restricted to once per star, thus two times in total. This would allow us to hop between the science and reference stars approximately every ten minutes without much loss in photon collecting efficiency, thereby ensuring minimal change in PSF shape in the elapsed time. We do not provide an exact calculation for the optimum hopping frequency as it depends strongly on how the seeing and coherence time vary

<sup>2</sup> <https://github.com/zwahhaj/starhopping>

over the observation. However, we found in our observations that PSF similarity drops  $\sim 2\%$  every ten minutes (see Sect. 3.3). This is significant as the sensitivity reached depends nonlinearly on the PSF subtraction quality. Thus, we recommend observing the science target for ten minutes, then hopping to the reference star and observing it for five minutes, repeating the cycle as needed.

To preserve PSF similarity and for time efficiency, the AO loops would not be re-optimized when changing stars, and thus the reference star would need to have an  $R$  magnitude (mag) within 1 mag of the science star, to ensure similar AO performance. While we do not have strong constraints on the color of the reference star, again similar brightness (within 1 mag) in the observing wavelength is important. This is because the AO performance needs to be similar and the signal-to-noise ratio (S/N) of the reference images need to be comparable or better. Also, the reference star would need to be within 1 to 2 degrees of the science star, so that the shape changes of the main mirror at the new pointing would not result in large changes in PSF properties. Fortunately, for the vast majority of stars fainter than  $R \sim 4$  mag a suitable reference star can be found, making star-hopping practical for  $R \sim 4$ –13 mag stars. The solution required new software to be designed for telescope control and new template software to be written for the observing sequence and instrument, that is, SPHERE's control.

For SPHERE, we designed two new acquisition templates called *starhop* and *hopback*, which are only responsible for moving the telescope between the two stars and store relevant setup information so that subsequent hops can be made automatically. Thus a typical observing sequence is as follows: (1) Normal acquisition of science star with desired instrumental mode and setup; (2) an observing template lasting a few minutes; (3) acquisition of a reference star a few degrees away, with the *starhop* template; (4) another observing template; (5) quick return to the science star using the *hopback* template lasting approximately one minute; (6) another observing template; (7) quick return to reference star using the *hopback* template again; and (8) as many iterations of steps 4 to 7 as desired.

All three types of acquisitions constitute a full preset of the telescope, that is, the shape of the primary mirror and the pointing of the secondary are set by a look-up table, then a guide star is selected (automatic for *hopback*) for accurate pointing corrections and continuous active optics corrections for the main mirror shape are activated using the guide star. However, human operators only assist with the first (normal) acquisition and the *starhop* acquisition, especially in the selection of the guide star and related setup. The *starhop* template stores all parameters required for these setups for the first star, moves (presets) to the second star, lets the operator assist in the second acquisition, and then stores all the parameters for the second acquisition. Small telescope offsets for fine-centering made by the operator when positioning the star on the instrument detector are also recorded. Thus, the *hopback* template already has the relevant parameters saved and can automatically hop back and forth between the two stars, taking approximately one minute each time.

## 2.2. HR 8799 observations

We observed HR 8799 as part of a director's discretionary time (DDT) proposal to test the performance limits of star-hopping with RDI on SPHERE. The SPHERE instrument (Beuzit et al. 2019), installed at the Nasmyth Focus of unit telescope 3 (UT3) at the VLT, is one of the most advanced high-contrast imagers to date. It is also a polarimeter and spectrograph that is designed to find and characterize exoplanets. It employs an extreme AO

system called SAXO (Fusco et al. 2005, 2006; Petit et al. 2012; Sauvage et al. 2016) with  $41 \times 41$  actuators (1377 active in the pupil) for wavefront control, a low read noise EMCCD running at 1380 Hz, a fast (800 Hz bandwidth) tip-tilt mirror (ITTM) for pupil stabilization, extremely smooth toric mirrors (Hugot et al. 2012), and a differential tip-tilt loop for accurate centering in the NIR. This system can deliver  $H$ -band strehl ratios for bright stars ( $R < 9$ ) of up to 90% and continue to provide AO correction for stars as faint as  $R = 14$  mag. The SPHERE instrument also provides coronagraphs for diffraction suppression, including apodized Lyot coronagraphs (Soummer 2005) and achromatic four-quadrants phase masks (Boccaletti et al. 2008). It is comprised of three subsystems: the infrared dual-band imager and spectrograph (IRDIS; Dohlen et al. 2008), an integral field spectrograph (IFS; Claudi et al. 2008) and the ZIMPOL imaging polarimeter (ZIMPOL; Schmid et al. 2018).

We observed HR 8799 in the IRDIFS extended mode (Zurlo et al. 2014), where IRDIS  $K1$  and  $K2$ -band images and IFS  $Y$ - $H$  spectra are obtained simultaneously (Vigan et al. 2010). The IRDIFS data was obtained in three 1.5 h observing blocks (OBS): one block on the night of October 31 2019 and two contiguous blocks on the night of November 1, 2019. We used the N\_ALC\_YJ\_S coronagraph with a central obscuration of radius 73 mas, which is not ideal for the maximum contrast in  $K$  band but ensures that any object at 100 mas separation would not be partially obscured. With IRDIS we used 8 s exposures, while with IFS we used 32 s. We also obtained short-exposure unsaturated non-coronagraphic observations of the primary star for flux calibration, which we henceforth call FLUX observations. The data sets can be found in the ESO archive under program ID 2103.C-5076(A) and container IDs 2622640, 2623891, and 2623923. Each container represents a separate epoch, consisting of several OBS alternating between HR 8799 and the reference star. The reference star, HD 218381 (spectral type K0 versus F0V for HR 8799), is separated  $0.55^\circ$  from HR 8799 and is 0.52 mag fainter than it in the  $R$  band but 0.75 mag brighter in the  $H$  band. In total, we had 1440 IRDIS exposures for HR 8799 and 830 for the reference star. With IFS, we had 190 exposures for HR 8799 and 114 for the reference star. The observing conditions were average, with a coherence time of  $4.7 \pm 1.3$  ms, a seeing of  $0.9 \pm 0.15''$ , and a windspeed of  $2.1$ – $7.7$   $\text{m s}^{-1}$  without the low-wind effect (Milli et al. 2018). The total sky rotations were  $23.8^\circ$  on the first night and  $53.4^\circ$  on the second night.

## 3. Data reduction

### 3.1. IFS reduction and contrast limit estimates

Since our main motivation is to achieve sensitivities to fainter planets than earlier observations, we began by estimating the detection limits of our data set and post-processing method. The detection limits were estimated by comparison to simulated planets that undergo the same reduction processes as the real planets. The measurement and analysis of the real planets in the system are presented afterward. For the basic reduction calibrations, we used SPHERE pipeline version 0.36.0 and scripts<sup>3</sup> by Vigan et al. (2015). The IFS data sets from all three epochs were combined to form a cube of 7254 images with 186 images in each of the 39 wavelength channels. In each image, 16 simulated companions were inserted with offsets from the star, given by separations  $0.1''$  to  $1.6''$  with steps of  $0.1''$  and position

<sup>3</sup> <http://astro.vigan.fr/tools.html>

angles (PAs) increments of  $90^\circ$  with each step. The simulated companions were made from the FLUX exposures of the primary appropriately scaled in intensity. Since these sources were given constant chromatic contrast (that is, the same spectra as the host star), we did not apply any spectral differencing in the reduction described below. The contrasts of these sources were chosen to be roughly 2 mag brighter than a preliminary contrast limit estimate for the data set. The reference PSF data set consisted of 4446 images. All science and reference images were unsharp masked, that is, each image was convolved with a Gaussian of full width at half maximum (FWHM)  $0.1''$  (roughly twice the image resolution) and subtracted from the original to produce an image in which most large-scale spatial features such as diffuse stellar light have been removed (e.g., Racine et al. 1999; Wahhaj et al. 2013).

A diagonally oriented stripe pattern was found in all the IFS images, which we were unable to remove in the basic calibrated images. A zero-valued image passed through the basic calibration also yielded this pattern and found to be independent of the channel wavelength. Thus the pattern is likely an artifact of the pipeline. The output pattern image was bad-pixel cleaned and unsharp-masked to prepare it to be subtracted from the science images. Two annular regions were defined to optimize PSF subtraction, that is, minimize the residual RMS in each region. These two annuli had inner and outer radii of  $0.075''$  and  $0.67''$ , and  $0.67''$  and  $1.33''$ , respectively. The science images were median-combined without de-rotation to reveal the background stripe pattern more clearly. Then we obtained the best intensity-scaled pattern images for the inner and outer annuli, which we in turn subtracted from each science image, to perform a preliminary removal of the pattern. Next, for each science image, we computed the best linear combination of reference images that reduced the RMS in the two annular regions separately, similar to the LOCI algorithm (Lafrenière et al. 2007), but this was a much simpler version since optimization is done only over the two large annuli. We then took the difference of the science image and this composite reference image and further applied an azimuthal profile removal filter as described in Wahhaj et al. (2013). All the difference images were median-combined, and any residual striped pattern in the resultant image was removed again via the same procedure as before.

Generally, we see a consistent but modest improvement in contrast ( $\sim 0.2$  mag) with the use of image filters (e.g., unsharp masking), and so we recommend their use. Also, we notice fewer artifacts, for example, fewer PSF residuals in these reductions. However, as data sets may differ in PSF morphology, we also recommend studying reductions without applying such filters, even when trying to detect faint point sources.

Next, the images were derotated to align the sky with north up and east left orientation and median-combined. A S/N map is made for the final reduced image (Fig. 1), where the pixels in annular rings of width 4 pixels are divided by the robust standard deviation in that region. The robust value is taken to mitigate the effect of the simulated planets on the RMS. The S/N of each recovered simulated planet was then compared to its input contrast to calculate the  $5\sigma$  contrast limit achieved at the separation, given as  $\text{Contrast} = \text{InputContrast} \times S/N/5$ . The  $5\sigma$  contrasts achieved in this RDI-only reduction at  $0.1''$ ,  $0.2''$ ,  $0.4''$ , and  $0.8''$  separations were 11.2, 13.5, 14.4, and 15 mag corresponding to mass limits of 6.5, 3.1, 2.3, and  $1.8 M_{\text{Jup}}$  respectively, as estimated from BT-Settl models assuming an age of 30 Myr (Allard et al. 2012b). The contrast curve is shown in Fig. 2. The reduction showing only the real planets (without sim-

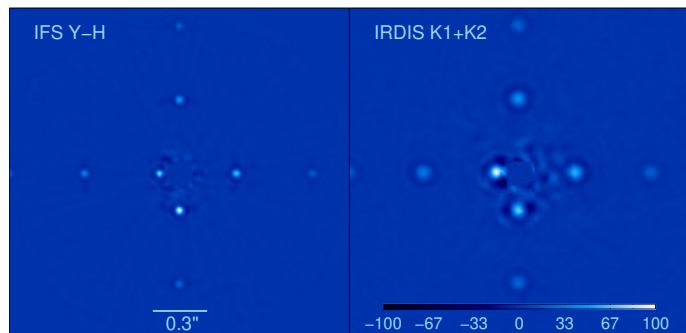


**Fig. 1.** Recovery of simulated planets. *Left*: an IFS  $Y-H$  band reduced image showing simulated planets recovered with high S/N. The source recovered closest to the star indicates a contrast limit of 11.2 mag at  $0.1''$  projected separation. *Right*: an IRDIS  $K1+K2$  band reduced image also showing simulated planets at the same separations, all recovered with high S/N. The same contrast at  $0.1''$  was reached with IRDIS also. The planets were inserted into the basic calibrated data (flat-fielded, dark-subtracted, and bad pixel corrected) All real planets have been masked out. The color scale is linear with intensity.

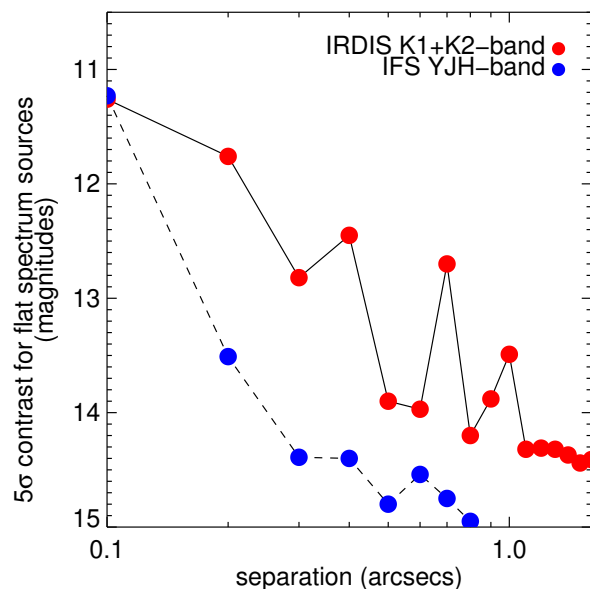


**Fig. 2.** Contrast limits achieved in the IFS and IRDIS data sets, estimated by flux comparison to simulated planets recovered post-reduction.

ulated planet insertions) is shown in Fig. 3. No new planets are detected.

### 3.2. IRDIS reduction and contrast limit estimates

The IRDIS reductions with simulated planets were done in a similar way to the IFS reductions. Since there were less images to process, we opted to use a more sophisticated but also more computation intensive reduction method. The simulated planets were inserted in the basic calibrated data at the same offsets with respect to the star as before. The planets inserted were  $\sim 1$  mag brighter than the  $5\sigma$  detection limit. For this exercise, we did not correct the relative rotational offset between IFS and IRDIS, so the PAs of the real HR 8799 planets do not agree between the two reduced images in Fig. 1. There were 1443 good science images in the three data sets combined and 828 reference images.

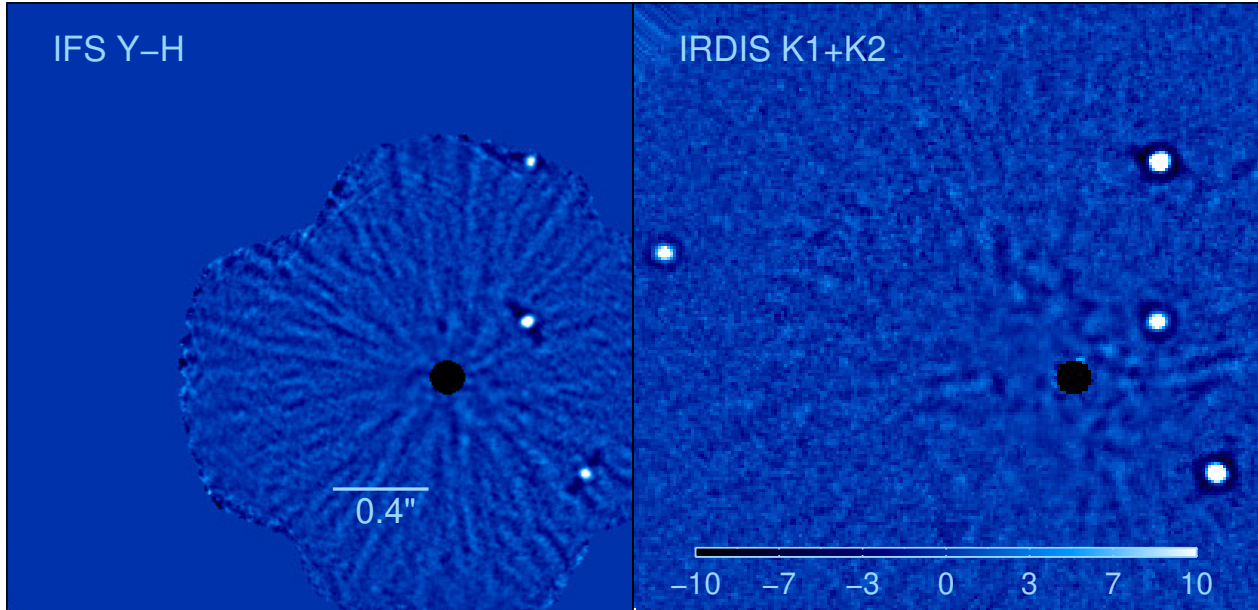


**Fig. 3.** IFS and IRDIS images from star-hopping RDI reductions shown with same scale and orientation (North is up, east is left). *Left:* S/N map of the IFS  $Y-H$  band reduced image, showing only the real planets. The azimuthal filtering creates the dark negative arcs around the planets. They are more pronounced in the IFS reduction because more images were combined than for the IRDIS reduction. *Right:* S/N map of the IRDIS  $K1 + K2$  band reduced image, showing only the real planets. The star, at the center of the black circle, is masked by the coronagraph. No new planets are detected in the newly probed region around  $0.1''$  separation above the contrast limit of 11.2 mag.

The images were first unsharp-masked. Next, we calculated the residual rms between all pairs of science and reference images, after intensity scaling to minimize the rms between 70 mas and 270 mas. For each science image, the best 16 reference images (more would worsen signal loss) were linearly combined by LOCI for subtraction to minimize the residual rms separately in annular rings covering the whole image. Each target annulus, where the subtraction was done, had a 200 mas width. But the reference annuli, where LOCI tried to minimize the residual rms, started 25 mas outside the target annuli and extended outward to cover the rest of the image. This was done to mitigate over-subtraction and signal loss. We chose these parameters mostly by trial and error. The azimuthal filtering, deroation and combination of all the difference images, and the contrast limit estimates were done in the same way as in the IFS reduction. The final reduced images (with and without simulated companions) and the contrast performance are shown in Figs. 1–3, respectively. The IRDIS contrast limit is 11.2 mag at  $0.1''$ , which is equal to the IFS limits, but IFS fares  $\sim 0.5$  mag better at larger separations.

### 3.3. Comparison of RDI and ADI IRDIS detection limits

For a comparison of typical ADI and RDI IRDIS observations we used only the first of the three data sets, totalling 1.5 h of execution time, since this is slightly longer than the typical observation length (1 h) at the VLT. The data set constitutes 481 science images and for RDI, 276 reference images. The total sky rotation in the sciences images was  $24^\circ$ . We performed three different ADI-based reductions, which we call *ADI-LOCI-F1*, *ASDI-LOCI-F10*, and *ASDI-PCA-F10*. The *ADI-LOCI-F1* is the same as the RDI reduction in terms of reference image selection and reference sector size and the use of LOCI, except that the references were restricted to those with more relative rotation than one-half FWHM (found by trial). The *ASDI-LOCI-F10*

reduction was performed on a data set with simulated companions which were made ten times fainter (thus labeled *F10*) in the  $K2$  channel than in  $K1$  channel, allowing aggressive spectral differencing and a potential contrast gain over ADI. Since reference images could have companions that are spectrally and rotationally displaced, only the combined displacement needs to be more than one-half FWHM. The *ASDI-PCA-F10* reduction was performed on the same data set as that of *ASDI-LOCI-F10*. The reduction parameters were again optimized by trial and error. We used principal component analysis (PCA) to construct the subtraction PSFs with five components (see Soummer et al. 2012). However, for each science image and for each annular subcomponent of the image (same as the reductions above) only selected subsets of the science images were chosen as inputs for the PCA. The residual rms were calculated after subtracting all science image pairs, the best 30 matches (with least rms) that had more relative rotation than one-half FWHM were chosen. If less than 30 appropriate matches were found, then the relative rotation criteria was relaxed to down to one-fourth FWHM, but no further, to allow input images for the PSF construction. This more selective approach to PCA helps us reduce the signal self-subtraction expected in ADI; our tests supported this assumption, yielding significantly better results than PCA alone.

The RDI reduction (see top of Sect. 3.2) was repeated for the same 1.5 h data set used in the ADI reduction. In Fig. 4 we compare the RDI and the *ADI-LOCI-F1* reduction. The simulated planets inside  $0.3''$  separation are much better recovered in the star-hopping RDI reduction. In the ADI reduction, the innermost planet at  $0.1''$  is not recovered at all, while the one at  $0.2''$  is barely recovered. Contrast curves were calculated from the S/N of the recovered simulated planets as before. The contrast improvement of RDI over the three ADI reductions, more than 2 mag at  $0.1''$  separation, is shown in Fig. 5 as a difference between the two contrast curves. The improvement of course varies with the total amount of sky rotation in the science images.

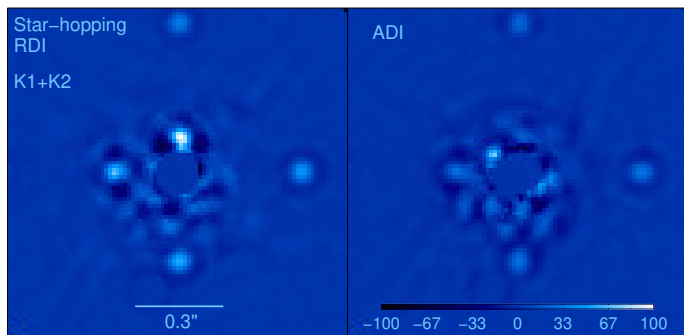


**Fig. 4.** Comparison of star-hopping RDI vs. ADI reductions of IRDIS K1 + K2 band data injected with flat spectrum simulated planets. The inner two simulated planets are not successfully recovered in the ADI reduction, while they are clearly detected in the RDI reductions. The third simulated planet is recovered significantly better in the star-hopping RDI reduction. All real planets are masked out. The color scale is linear with intensity.

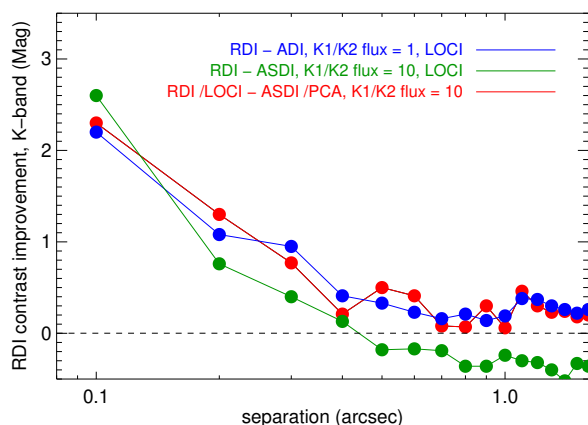


**Fig. 5.** Contrast improvement using RDI over ADI or ASDI, estimated from the S/N of recovered simulated companions from an IRDIS data set. The star-hopping RDI technique yields detection limits more than 2 mag fainter than ADI at 0.1 separation from the target star. The green line shows the case for a K1/K2 companion flux ratio of 10 and very similar algorithms for RDI and ASDI, except that the ASDI reduction is fine-tuned to minimize self-subtraction. The blue line similarly shows RDI–ADI difference for equal K1, K2 flux. The red line shows the RDI improvement against the best PCA-based ADI reduction for a K1/K2 flux ratio of 10. The LOCI and PCA reductions are described in Sect. 3.3.

Figure 7 illustrates why star-hopping RDI performs so much better than ADI. This figure shows the residual fractional rms (RFR) for each science image as a function of relative rotation, that is, the remaining rms between 0.1''–0.3'' separations after subtraction of another science or reference star image, divided by the original rms in each science image. Specifically,  $RFR_i = \text{RMS}(s_i - o_j) / \text{RMS}(s_i)$ , where  $s_i$  is a science image,  $o_j$  is another science or reference star image and RMS is computed between 0.1''–0.3'' separations. The RFRs post-RDI subtraction had a  $2\sigma$  range of 0.32–0.78. We see that although the science images provide better-matched PSFs in general, the images that can be used with minimal self-subtraction are much fewer and much poorer matches than the RDI reference set. Thus, the reference star images constitute a superior set for constructing subtraction PSFs.

In Fig. 6 we show that artificially increasing the field rotation for the RDI reduction (1.5 h data set) before coadding the

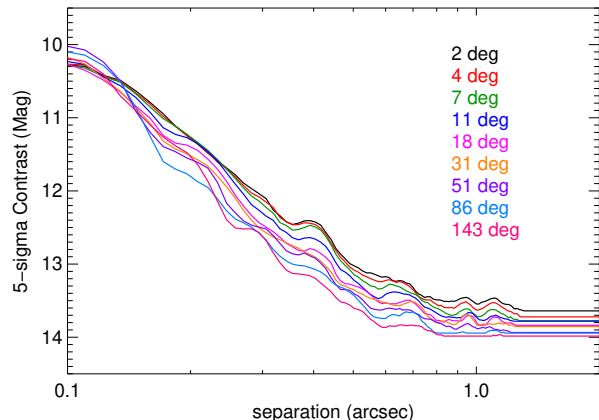


**Fig. 6.** Artificially increasing the field rotation for an RDI reduction before coadding the images does not improve the contrast significantly (see Sect. 3.3). The legend gives the total rotation of the reduction for each contrast curve. No improvement is seen at small separations (0.1–0.2'') because contrasts are not correlated with rotation angles. At larger separations, a maximum of 0.5 mag improvement is seen between the minimum and maximum rotations, 2° and 143°, but only 0.3 mag improvement between 18° and 143°.

images does not significantly improve the contrast. Thus the speckle residuals are comparable to white noise as more rotation does not seem to result in additional smoothing. We estimate no improvement at 0.1'', ~0.2 mag improvement farther out when comparing rotations of 140° to 20°, and 0.5 mag improvement at 1'', when comparing rotations of 140° to 2°. The reductions were done by multiplying the actual PAs of the images by specific factors that would achieve total field rotations of 2° to ~140° (distributed logarithmically), before coadding the images.

During star-hopping tests on the night of August 8, 2019, we obtained eight images for each of a pair of stars, HD 196963 and HD 196081, which are separated by  $\sim 1.75''$ . Since this pair has a much larger angular separation, we can use the RFR from this data set to gauge whether there is significant degradation in PSF similarity. Fortunately, the  $2\sigma$  range of the RFR was 0.33–0.53, indicating that star-hopping is still very effective for such large separations. It should be noted that the coherence time was only 1.9–2.1 msec for these observations, compared to 2.5–7.2 msec for the HR 8799 observations. Although we have low statistics for such a performance, these results show that even in poor to average conditions, star-hopping RDI can be effective for a pair of stars separated by almost 2°.

### 3.4. JH-band spectra from IFS

The spectra of planets *c*, *d*, and *e* were extracted with an aperture size of 3 pixels for all IFS channels. The spectra for planets *d* and *e* were corrected for flux loss by comparing them to three flat contrast sources (uniform contrast across wavelength) per planet inserted at the separations of the planets, but at different PAs (offset from the planets by 30° to 270°). These simulated planets are just the IFS FLUX exposures scaled appropriately in intensity. They were inserted at 10 mag of contrast, which is somewhat brighter than the real planets. Since planet *c* was detected at the edge of the IFS detector where simulated planets could not be inserted, we used the same comparison sources for planets *c* and *d*. The simulated planets undergo the same reduction process as the real planets, their fluxes are extracted using the same aperture sizes, and thus their systematic fractional flux error are the

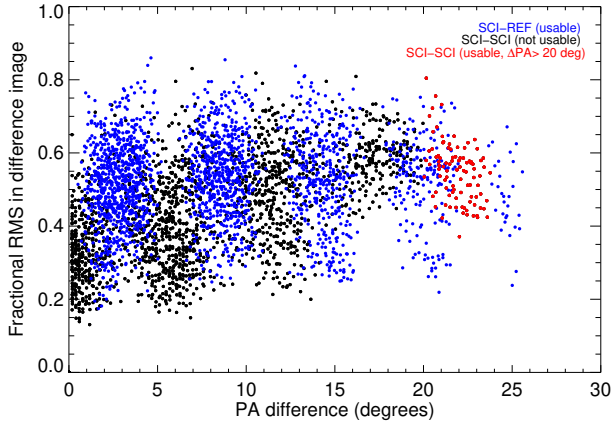


**Fig. 7.** Comparison of PSF similarity between reference-science and science-science pairs. The residual fractional rms of difference images are plotted as a function of relative PA/rotational offset. The black dots represent science-science subtractions, the blue dots represent science-reference subtractions, and the red dots represent science-science differences with acceptable self-subtraction. For the science-reference points, the relevant quantity is the time difference, which has an almost linear relationship to the PA difference.

same. We verified this by checking that the spectrum recovered from the simulated companions had a uniform contrast. Thus the planet spectra is calculated as

$$B_{\text{PR}}(\lambda) = \frac{F_{\text{PR}}(\lambda)}{F_{\text{PS}}(\lambda)} \times 10^{-4} B_{\text{S}}(\lambda), \quad (1)$$

where  $F_{\text{PR}}$  and  $F_{\text{PS}}$  are the real and simulated planet aperture fluxes, respectively, and  $B_{\text{S}}$  is the stellar spectra. Here, the fractional flux losses for the real planet are fully accounted for in the ratio  $F_{\text{PR}}(\lambda)/F_{\text{PS}}(\lambda)$ .

The flux corrected spectra for planets *d* and *e* are shown in Fig. 8 along with that of the particularly red L6 object 2MASS J2148+4003 (Looper et al. 2008) for comparison. All three spectra are much redder toward the *H* band, in comparison to typical late L-types. Although not as red, the dusty dwarves of the field population also have redder than average spectra (see Zurlo et al. 2016; Stephens et al. 2009; Gagné et al. 2014). It should be noted that the spectra differ somewhat in shape from earlier publications, (e.g., Zurlo et al. 2016). This could be because the spectra we present in this work are the first not to be affected by signal self-subtraction due to ADI or SDI processing. The most notable differences from earlier spectra (see Fig. 9) are less defined peaks at 1.1  $\mu\text{m}$ , and for planet *d* in 2019, a gentler slope toward 1.6  $\mu\text{m}$ . The absence of the peak at 1.1  $\mu\text{m}$  is common among observed late L-type (see Fig. 3 of Bonnefoy et al. 2016, for example) as well as in the spectra of 2MASS J2148+4003. However, we also note that the 2016 spectral slopes toward 1.6  $\mu\text{m}$  are very similar to planet *e* in 2019. Although, the higher fluxes at 1.6  $\mu\text{m}$  are rarer among such L-types, it would explain the earlier discrepancy between IRDIS and IFS fluxes near the *H* band (Zurlo et al. 2016). We could not estimate an accurate flux normalization for the spectra of planet *c* as it was detected near the edge of the detector, so we show its spectra normalized to 1 at 1.25  $\mu\text{m}$  in Fig. 10. We do not pursue this further, as accurate *JH*-band photometry has already been provided in past publications. However, the shape of the planet’s spectra is reliably detected and shows an even redder *J – H* color than planets *d* and *e*. Although such red spectra are not common, a very similar slope (flux doubling between 1.25 and 1.6  $\mu\text{m}$ ) was seen in

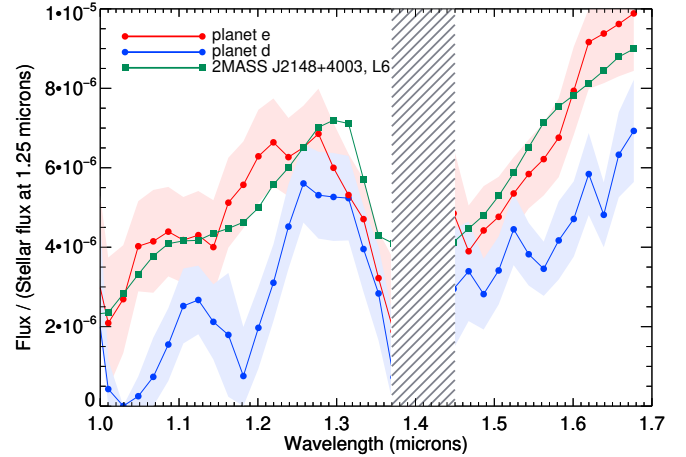


**Fig. 8.** Spectra for planets *d* and *e* compared with that of the L6 object, 2MASS J2148+4003 from Looper et al. (2008). The planet spectra have been divided by the stellar flux at 1.25  $\mu\text{m}$  to show the contrast at that wavelength. The L6 object spectra has been scaled to match planet *e* at 1.25  $\mu\text{m}$ . The shaded regions indicate the  $1\sigma$  error ranges of the spectra. The wavelength range 1.37–1.45  $\mu\text{m}$ , which is dominated by telluric lines, is not shown.

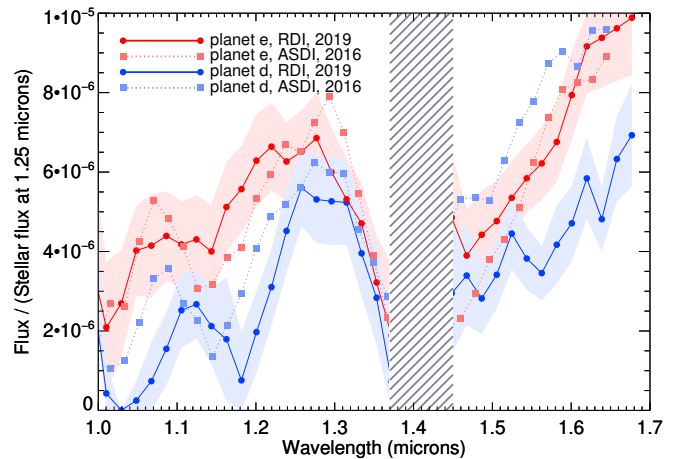


**Fig. 9.** Spectra extracted by RDI for planets *d* and *e* in 2019 compared with their ADI-extracted spectra from 2016 as reported in Zurlo et al. (2016). The 2016 and 2019 planet spectra are matched at 1.25  $\mu\text{m}$  for easier comparison of their shapes. The shaded regions indicate the  $1\sigma$  error ranges of the spectra. The wavelength range 1.37–1.45  $\mu\text{m}$ , which is dominated by telluric lines, is not shown.

the L7 object, VHS J125601257 b (Gauza et al. 2015). This L7 object, a planetary candidate companion to a brown dwarf, is also thought to have a dusty atmosphere with thick clouds (see Bonnefoy et al. 2016, for a discussion).

### 3.5. The HR 8799 debris disk

Booth et al. (2016), using the ALMA millimeter array, detected a broad debris ring, extending from  $\sim 145$  au to  $\sim 430$  au with an inclination of  $40 \pm 6^\circ$  and a PA of  $51 \pm 8^\circ$ . Prior to this, Su et al. (2009) inferred from the spectral energy distribution of the system that a planetesimal belt extending from 100 au to 300 au separation was the source of blow-out grains extending out to  $\sim 1500$  au. Thus the inner radius of the disk could start as close as 2.5'' and the outer radius could be as far as 11'' from the star.

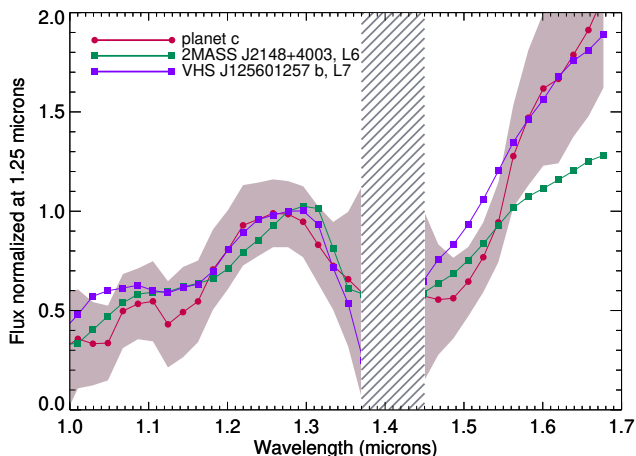


**Fig. 10.** Spectra extracted by RDI for planet *c* compared with that of the L6 object, 2MASS J2148+4003 from [Looper et al. \(2008\)](#) and L7 object VHS J125601257 b from [Gauza et al. \(2015\)](#). The wavelength range 1.37–1.45  $\mu\text{m}$ , which is dominated by telluric lines, is not shown.

It is expected that RDI reductions would be a major improvement over ADI for detections of disks with large angular extents, as self-subtraction in these cases is a severe problem for ADI. To detect the disk, we repeated the IRDIS RDI reduction without simulated companions or any prior image filtering (used to enhance speckle subtraction) because these remove all extended emission. We only used the *K1*-band images as the *K2*-band images have a much higher background. Detecting disks that are close to azimuthally symmetric in the plane of the sky, and extended over several arcseconds is a challenge very different from planet recovery because the expected signal area is most of the image and the background area is perhaps nonexistent. The image sectors used for PSF subtraction cannot be small, as this would remove extended signal. So, we used one large annulus extending from 0.4'' to 2'' separations to cover most of the PSF halo. The final reduction is shown in Fig. 11, but no disk emission was detected down to a  $5\sigma$  contrast of 14.1 mag beyond 2.5'' separations. The non-detection is not surprising given the marginal detection of the much brighter 49 Cet debris disk with SPHERE ([Choquet et al. 2017](#)). The fractional disk luminosity of HR 8799 is  $8 \times 10^{-5}$  ([Su et al. 2009](#)) vs.  $9 \times 10^{-4}$  for 49 Cet ([Moór et al. 2015](#)). The inner radius of the disks start at roughly 2'' separation for both ([Choquet et al. 2017](#); [Booth et al. 2016](#)), with expected physical separations of 100–150 au. The two stars have similar spectral types (F0–A1) with very similar *H*-band magnitudes (5.3–5.5 mag).

### 3.6. IRDIS *K1*- and *K2*-band photometry

The photometry of the four planets were extracted by comparison with simulated planets in a similar way to the IFS spectra. For each of the four planets, three simulated planets were inserted into the data set with a contrast of 10 mag, at the same separation as the real planets, but with large PA offsets (30 to 270°). The relative aperture photometry was done similar to IFS, but with aperture radius 4 pixels, because of the larger FWHM in the *K* band. The recovered photometry are all brighter than the [Zurlo et al. \(2016\)](#) measurements by about 0.1 mag (see Table 1). The standard deviation in the contrasts estimates for the three reference simulated planets is less than 0.03 mag. The dominant contrast uncertainty comes from the measurement of the

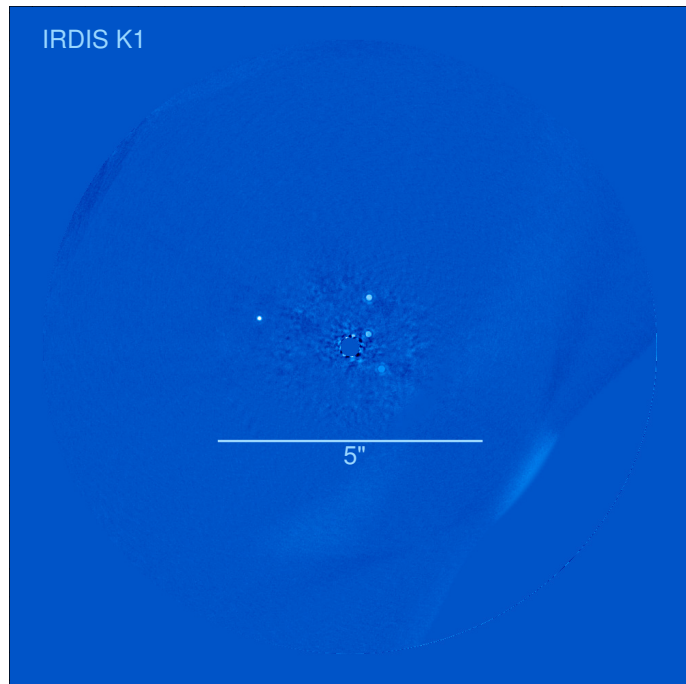


**Fig. 11.** IRDIS reduction without any prior image filtering to search for an extended circumstellar disk beyond angular separations of 2.5'' (to  $>6''$ ) from the star. [Booth et al. \(2016\)](#) ALMA observations indicate that the disk should have a PA of  $51 \pm 8^\circ$  and an inclination of  $40 \pm 6^\circ$ . No disk is detected down to a contrast limit of 14.1 mag. Some faint thermal emission from the detector background is seen in the bottom right, but not in the expected orientation of the known disk. North is up and east is to the left.

AO-corrected stellar PSF core flux, which is measured only once every 1.5 h.

### 3.7. Astrometric measurements and comparison to orbital models

The IRDIS data set for science images were reduced separately by the SPHERE data center ([Delorme et al. 2017](#)), which treated the data set as an ordinary pupil-tracking sequence. The data center applied the optimal distortion correction methods consistent with [Maire et al. \(2016\)](#) to produce a basic-calibrated data set with high astrometric fidelity (3–4 mas). These images were then reduced using the high-contrast imaging algorithm, ANDROMEDA ([Cantalloube et al. 2015](#)), to produce astrometric measurements (see Table 1) for the four known HR 8799 planets. We also compared the recovered coordinates for the real planets between the RDI and ADI reductions, and found that the planet locations agreed to within 2.7 mas, smaller than the errors estimated in Table 1.

An exhaustive orbital fitting effort is currently being undertaken by Zurlo et al. (in prep.) including all extant astrometry. Moreover, extensive work has been done to find orbital solutions to the prior astrometry for this system, so we just compare our latest measurements to the viable orbits computed by [Wang et al. \(2018\)](#). From millions of orbits generated by a Monte Carlo method, these authors generated three sets of solutions: (1) The orbits are forced to be coplanar and have 1:2:4:8 orbital commensurabilities. (2) The orbits are not coplanar but have low eccentricities and period commensurabilities as before. (3) The orbits have no additional constraints. In Fig. 12, we overlay our

**Table 1.** Astrometry and photometry of the four HR 8799 planets.

planet	$\rho$ (mas)	$\sigma_\rho$ (mas)	PA	$\sigma_{PA}$	$S/N$	$\Delta K1$ (mag)	$\Delta K2$ (mag)	Mass ( $M_J$ )
<i>e</i>	406	4	302.72°	0.04°	41	10.8 ± 0.02	10.63 ± 0.03	8 <sup>+7</sup> <sub>-2</sub>
<i>d</i>	686	4	231.38°	0.006°	83	10.7 ± 0.02	10.47 ± 0.02	8 <sup>+7</sup> <sub>-2</sub>
<i>c</i>	958	3	335.86°	0.05°	96	10.8 ± 0.02	10.53 ± 0.03	8 <sup>+7</sup> <sub>-2</sub>
<i>b</i>	1721	4	69.05°	0.04°	47	11.89 ± 0.01	10.75 ± 0.01	6 <sup>+7</sup> <sub>-1</sub>

**Notes.** The mass estimates are from the PHOENIX BT-Settl atmospheric models (Baraffe et al. 2015), assuming an age of 30<sup>+130</sup><sub>-10</sub> Myr. However, the most dynamically stable orbital solutions from Wang et al. (2018) set much tighter limits: a mass of 5.8 ± 0.5  $M_J$  for planet *b*, and 7.2 ± 0.6  $M_J$  for the other planets.

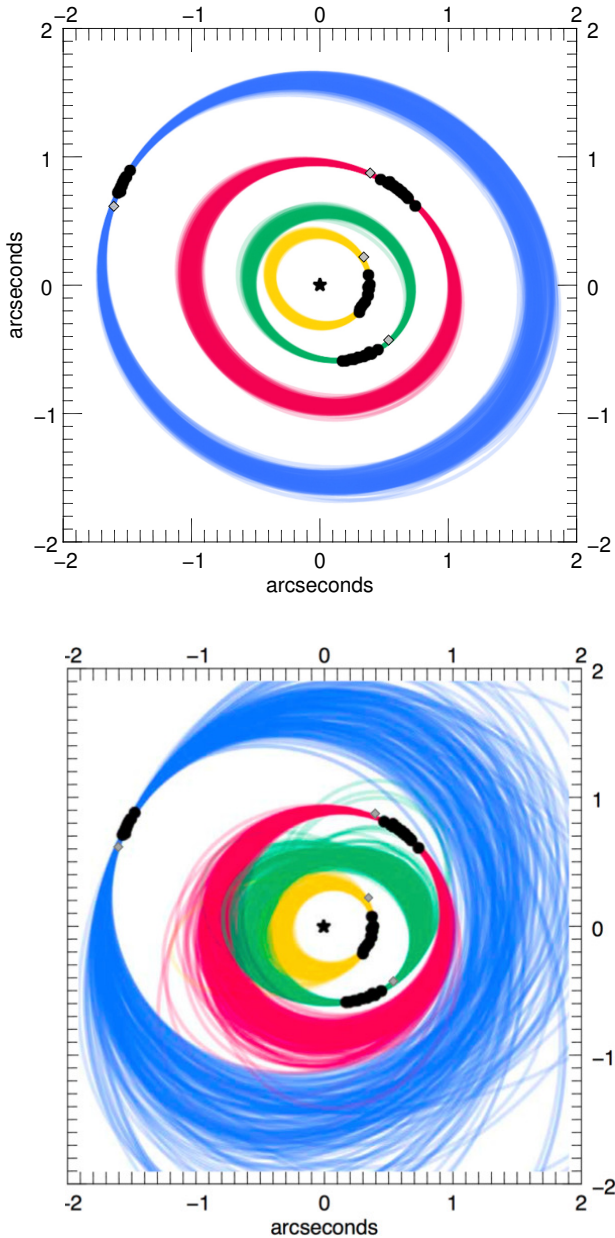


**Fig. 12.** Orbital models and planet astrometry. *Top:* November 1, 2019 epoch astrometry overlaid as gray diamonds on the most dynamically stable orbital solutions from Wang et al. (2018; see their Fig. 4), where coplanarity and 1:2:4:8 period commensurabilities were imposed. The black dots represent earlier measured astrometry for the four planets. *Bottom:* Same points overlaid on the orbital solutions without the additional constraints. The 2019 locations for planets *e* and *c* are more consistent with the dynamically stable family of orbits.

astrometry on orbital solution sets 1 and 3. Although, the latest points are consistent with both sets of solutions, planets *e* and *c* fall close to the expected position in the dynamically stable set, but a bit far from the mean expected location in the unconstrained set of orbits. Thus, the coplanar orbits with period commensurabilities are favored in our comparisons.

Survival of the four planets and even a hypothetical fifth planet is possible for the lifetime of the system (>30 Myr), but requires the period commensurabilities mentioned above. This was needed even when only planets *b*, *c*, and *d* were known (Goździewski & Migaszewski 2009; Reidemeister et al. 2009; Fabrycky & Murray-Clay 2010; Marshall et al. 2010). Such dynamical models envision that the four planets were formed at larger separations and migrated inward. This would allow the very similar chemical compositions indicated by their spectra, as opposed to more variation expected if they had formed in situ (Marois et al. 2010).

The most likely semimajor axes allowed for the hypothetical inner planet *f*, estimated by Goździewski & Migaszewski (2014, 2018) were 7.5 au and 9.7 au, with dynamical constraints on the masses of 2–8  $M_{Jup}$  and 1.5–5  $M_{Jup}$  respectively. The IFS contrasts we achieved at these separation were 13.05 mag and 13.86 mag, corresponding to estimated masses of 3.6  $M_{Jup}$  and 2.8  $M_{Jup}$ , respectively (assuming an age of 30 Myr), from the BT-Settl models (Allard et al. 2012b). Thus, the planet may still exist with a mass of 2–3.6  $M_{Jup}$  at 7.5 au or 1.5–2.8  $M_{Jup}$  at 10 au.

#### 4. Conclusions

In this paper, we successfully used the new star-hopping RDI technique to detect all four known planets of the HR 8799 system and significantly improved on the contrast limits attained previously with ADI, at separations less than 0.4". This technique of moving quickly to a reference star to capture a similar AO PSF for differencing, with only a one minute gap in photon collection, can now be used in service mode at the VLT with all the observing modes available on the SPHERE instrument. Using star-hopping RDI, we demonstrated the contrast improvement at 0.1" separation can be up to 2 mag, while at larger separations the improvement can be ≈1–0.5 mag, the results of which are comparable to those of Ruane et al. (2019). With this technique there is no need for any local sidereal time constraints during observations, which is usually essential for ADI observations. This means that the observing window for typical targets can be expanded by a factor of 2–3. Moreover, star-hopping can usually be used for stars fainter than  $R = 4$  mag because for these objects a reference star of comparable brightness can be found within 1–2 degrees (closer is better). Indeed we found comparable PSF similarity for a pair of stars 1.75° apart. The technique provides significant contrast improvement mainly for

two reasons: The usable PSFs, those that when subtracted will not result in significant self-subtraction of astrophysical point sources, firstly, occur closer in time and thus are more similar to the target PSF than in ADI. Secondly, these PSFs are more numerous than in ADI because they are spread uniformly over the whole sequence, rather than only available after significant sky rotation. The benefit for extended objects like circumstellar disks will have most impact because in ADI the self-subtraction artifacts can result in significant change in their apparent morphology.

In our SPHERE observations of HR 8799, we did not detect planet *f* at the most plausible locations, 7.5 and 9.7 au, down to mass limits of 3.6 and 2.8  $M_{\text{Jup}}$ , respectively. Also, we did not detect any new candidate companions, even at the smallest observable separation, 0.1'' or  $\approx 4.1$  au, where we attained a contrast limit of 11.2 mag or 6  $M_{\text{Jup}}$  in *K1 + K2* band (6.5  $M_{\text{Jup}}$  in *JHK* band using BT-Settl models from Allard et al. 2012a). However, we detected all four planets in the *K1 + K2* band with S/N of 41, 83, 96, and 47 for planets *e*, *d*, *c*, and *b*, respectively. The *YJH* spectra for planets *c*, *d*, *e* were detected with very red colors. Our spectra of planet *c* has higher S/N than earlier observations (P1640; Oppenheimer et al. 2013; Pueyo et al. 2015). Planets *c* and *d* spectra have some differences with respect to earlier observations. Particularly, the spectral slope is redder in the *H* band, which is significant as that part of the spectra has the highest S/N. This could be due to real evolution of the atmosphere of the planets over the past few years. Previous work has already shown that it is difficult to find close matches between the planet spectra and current compositional models owing to inadequate understanding of cloud properties and non-equilibrium chemistry (Bonnetfoy et al. 2016). However, the spectra are matched very closely by some red field dwarfs and a planetary mass companion to a brown dwarf (VHS J125601.92-125723.9 b; Gauza et al. 2015). We did not detect the debris disk seen by ALMA (Booth et al. 2016), but this is not surprising given that the much brighter debris disk of a comparable system, 49 Cet, was only marginally detected by SPHERE (Choquet et al. 2017). Finally, comparing the current locations of the planets to orbital solutions from Wang et al. (2018), we found that planets *e* and *c* are more consistent with coplanar and resonant orbits than without such restrictions.

In summary, the star-hopping RDI technique significantly boosts the detection capabilities of SPHERE for planets and circumstellar disks and should contribute to high-impact exoplanet science as the technique is brought to other telescope facilities.

**Acknowledgements.** This work has made use of the SPHERE Data Centre, jointly operated by OSUG/IPAG (Grenoble), PYTHEAS/LAM/CESAM (Marseille), OCA/Lagrange (Nice), Observatoire de Paris/LESIA (Paris), and Observatoire de Lyon. We would especially like to thank Nadege Meunier at the SPHERE data center in Grenoble for the distortion-corrected reductions used for the astrometric measurements, Bartosz Gauza for providing the spectra of VHS J125601.92-125723.9 b, Jason Wang for allowing us to use the dynamical modeling figures from his publication, and Matias Jones, Florian Rodler, Benjamin Courtney-Barré, Francisco Caceres and Alain Smette at the VLT for technical help during the various phases of the development of the star-hopping technique.

## References

- Allard, F., Homeier, D., & Freytag, B. 2012a, *Phil. Trans. R. Soc. London Ser. A*, 370, 2765
- Allard, F., Homeier, D., Freytag, B., & Sharp, C. M. 2012b, in *EAS Pub. Ser.*, eds. C. Reylé, C. Charbonnel, & M. Schultheis, 57, 3
- Apai, D., Radigan, J., Buenzli, E., et al. 2013, *ApJ*, 768, 121
- Baines, E. K., White, R. J., Huber, D., et al. 2012, *ApJ*, 761, 57
- Baraffe, I., Homeier, D., Allard, F., & Chabrier, G. 2015, *A&A*, 577, A42
- Barman, T. S., Macintosh, B., Konopacky, Q. M., & Marois, C. 2011, *ApJ*, 733, 65
- Barman, T. S., Konopacky, Q. M., Macintosh, B., & Marois, C. 2015, *ApJ*, 804, 61
- Bell, C. P. M., Mamajek, E. E., & Naylor, T. 2015, *Proc. Int. Astron. Union*, 10, 41
- Beuzit, J. L., Vigan, A., Mouillet, D., et al. 2019, *A&A*, 631, A155
- Boccaletti, A., Chauvin, G., Baudoz, P., & Beuzit, J. L. 2008, *A&A*, 482, 939
- Boccaletti, A., Sezestre, E., Lagrange, A. M., et al. 2018, *A&A*, 614, A52
- Boccaletti, A., Di Folco, E., Pantin, E., et al. 2020, *A&A*, 637, L5
- Bohn, A. J., Kenworthy, M. A., Ginski, C., et al. 2020, *MNRAS*, 492, 431
- Bonnefoy, M., Marleau, G. D., Galicher, R., et al. 2014, *A&A*, 567, L9
- Bonnefoy, M., Zurlo, A., Baudino, J. L., et al. 2016, *A&A*, 587, A58
- Booth, M., Jordán, A., Casassus, S., et al. 2016, *MNRAS*, 460, L10
- Buenzli, E., Saumon, D., Marley, M. S., et al. 2015, *ApJ*, 798, 127
- Cantalloube, F., Mouillet, D., Mugnier, L. M., et al. 2015, *A&A*, 582, A89
- Chatterjee, S., Ford, E. B., Matsumura, S., & Rasio, F. A. 2008, *ApJ*, 686, 580
- Chauvin, G., Desidera, S., Lagrange, A. M., et al. 2017, *A&A*, 605, L9
- Choquet, É., Perrin, M. D., Chen, C. H., et al. 2016, *ApJ*, 817, L2
- Choquet, É., Milli, J., Wahhaj, Z., et al. 2017, *ApJ*, 834, L12
- Claudi, R. U., Turatto, M., Gratton, R. G., et al. 2008, *Proc. SPIE*, 7014, 70143E
- Cowley, A., Cowley, C., Jaschek, M., & Jaschek, C. 1969, *AJ*, 74, 375
- Crida, A. 2009, in *SF2A-2009: Proceedings of the Annual meeting of the French Society of Astronomy and Astrophysics*, eds. M. Heydari-Malayeri, C. Reylé, & R. Samadi, 313
- Currie, T., Burrows, A., Itoh, Y., et al. 2011, *ApJ*, 729, 128
- Delorme, P., Meunier, N., Albert, D., et al. 2017, in *SF2A-2017: Proceedings of the Annual meeting of the French Society of Astronomy and Astrophysics*, eds. C. Reylé, P. Di Matteo, & F. Herpin
- Dohlen, K., Langlois, M., Saisse, M., et al. 2008, *Proc. SPIE*, 7014, 70143L
- Dong, S., & Zhu, Z. 2013, *ApJ*, 778, 53
- Fabrycky, D. C., & Murray-Clay, R. A. 2010, *ApJ*, 710, 1408
- Fernandes, R. B., Mulders, G. D., Pascucci, I., Mordasini, C., & Emsenhuber, A. 2019, *ApJ*, 874, 81
- Fusco, T., Petit, C., Rousset, G., Conan, J. M., & Beuzit, J. L. 2005, *Opt. Lett.*, 30, 1255
- Fusco, T., Rousset, G., Sauvage, J. F., et al. 2006, *Opt. Exp.*, 14, 7515
- Gagné, J., Lafrenière, D., Doyon, R., Malo, L., & Artigau, É. 2014, *ApJ*, 783, 121
- Gaia Collaboration 2018, *VizieR Online Data Catalog*: I/345
- Galicher, R., Marois, C., Macintosh, B., Barman, T., & Konopacky, Q. 2011, *ApJ*, 739, L41
- Gauza, B., Béjar, V. J. S., Pérez-Garrido, A., et al. 2015, *ApJ*, 804, 96
- Geiler, F., Krivov, A. V., Booth, M., & Löhne, T. 2019, *MNRAS*, 483, 332
- Goździewski, K., & Migaszewski, C. 2009, *MNRAS*, 397, L16
- Goździewski, K., & Migaszewski, C. 2014, *MNRAS*, 440, 3140
- Goździewski, K., & Migaszewski, C. 2018, *ApJS*, 238, 6
- Haffert, S. Y., Bohn, A. J., de Boer, J., et al. 2019, *Nat. Astron.*, 3, 749
- Hinz, P. M., Rodigas, T. J., Kenworthy, M. A., et al. 2010, *ApJ*, 716, 417
- Howard, A. W., Marcy, G. W., Johnson, J. A., et al. 2010, *Science*, 330, 653
- Hughes, A. M., Wilner, D. J., Andrews, S. M., et al. 2011, *ApJ*, 740, 38
- Hugot, E., Ferrari, M., El Hadi, K., et al. 2012, *A&A*, 538, A139
- Ingraham, P., Marley, M. S., Saumon, D., et al. 2014, *ApJ*, 794, L15
- Janson, M., Bergfors, C., Goto, M., Brandner, W., & Lafrenière, D. 2010, *ApJ*, 710, L35
- Kepler, M., Benisty, M., Müller, A., et al. 2018, *A&A*, 617, A44
- Konopacky, Q. M., Barman, T. S., Macintosh, B. A., & Marois, C. 2013, *Science*, 339, 1398
- Konopacky, Q. M., Marois, C., Macintosh, B. A., et al. 2016, *AJ*, 152, 28
- Lafrenière, D., Marois, C., Doyon, R., Nadeau, D., & Artigau, É. 2007, *ApJ*, 660, 770
- Lagrange, A. M., Gratadour, D., Chauvin, G., et al. 2009, *A&A*, 493, L21
- Lagrange, A. M., Boccaletti, A., Milli, J., et al. 2012, *A&A*, 542, A40
- Liu, M. C. 2004, *Science*, 305, 1442
- Looper, D. L., Kirkpatrick, J. D., Cutri, R. M., et al. 2008, *ApJ*, 686, 528
- Macintosh, B., Graham, J. R., Barman, T., et al. 2015, *Science*, 350, 64
- Madhusudhan, N. 2019, *ARA&A*, 57, 617
- Madhusudhan, N., Burrows, A., & Currie, T. 2011, *ApJ*, 737, 34
- Maire, A. L., Bonnefoy, M., Ginski, C., et al. 2016, *A&A*, 587, A56
- Marleau, G. D., & Cumming, A. 2014, *MNRAS*, 437, 1378
- Marley, M. S., Saumon, D., Cushing, M., et al. 2012, *ApJ*, 754, 135
- Marois, C., Lafrenière, D., Doyon, R., Macintosh, B., & Nadeau, D. 2006, *ApJ*, 641, 556
- Marois, C., Macintosh, B., Barman, T., et al. 2008, *Science*, 322, 1348
- Marois, C., Zuckerman, B., Konopacky, Q. M., Macintosh, B., & Barman, T. 2010, *Nature*, 468, 1080
- Marshall, J., Horner, J., & Carter, A. 2010, *Int. J. Astrobiol.*, 9, 259

- Matthews, B., Kennedy, G., Sibthorpe, B., et al. 2013, *ApJ*, **780**, 97
- Matthews, B., Kennedy, G., Sibthorpe, B., et al. 2014, *ApJ*, **780**, 97
- Mayor, M., Marmier, M., Lovis, C., et al. 2011, *ArXiv e-prints* [arXiv:1109.2497]
- Milli, J., Mouillet, D., Lagrange, A. M., et al. 2012, *A&A*, **545**, A111
- Milli, J., Kasper, M., Bourget, P., et al. 2018, *Proc. SPIE*, **10703**, 107032A
- Moór, A., Ábrahám, P., Derekas, A., et al. 2006, *ApJ*, **644**, 525
- Moór, A., Kóspál, Á., Ábrahám, P., et al. 2015, *MNRAS*, **447**, 577
- Morley, C. V., Fortney, J. J., Marley, M. S., et al. 2012, *ApJ*, **756**, 172
- Moro-Martín, A., Malhotra, R., Bryden, G., et al. 2010, *ApJ*, **717**, 1123
- Müller, A., Keppler, M., Henning, T., et al. 2018, *A&A*, **617**, L2
- Nielsen, E. L., De Rosa, R. J., Macintosh, B., et al. 2019, *AJ*, **158**, 13
- Oppenheimer, B. R., Baranec, C., Beichman, C., et al. 2013, *ApJ*, **768**, 24
- Petit, C., Sauvage, J. F., Sevin, A., et al. 2012, *Proc. SPIE*, **8447**, 84471Z
- Pueyo, L., Soummer, R., Hoffmann, J., et al. 2015, *ApJ*, **803**, 31
- Racine, R., Walker, G. A. H., Nadeau, D., Doyon, R., & Marois, C. 1999, *PASP*, **111**, 587
- Raymond, S. N., Armitage, P. J., & Gorelick, N. 2010, *ApJ*, **711**, 772
- Reidemeister, M., Krivov, A. V., Schmidt, T. O. B., et al. 2009, *A&A*, **503**, 247
- Ruane, G., Ngo, H., Mawet, D., et al. 2019, *AJ*, **157**, 118
- Sadakane, K., & Nishida, M. 1986, *PASP*, **98**, 685
- Saio, H. 2019, *MNRAS*, **487**, 2177
- Saio, H., Bedding, T. R., Kurtz, D. W., et al. 2018, *MNRAS*, **477**, 2183
- Sauvage, J.-F., Fusco, T., Petit, C., et al. 2016, *J. Astron. Telescopes Instrum. Syst.*, **2**
- Schmid, H. M., Bazzon, A., Roelfsema, R., et al. 2018, *A&A*, **619**, A9
- Skemer, A. J., Hinz, P. M., Esposito, S., et al. 2012, *ApJ*, **753**, 14
- Soummer, R. 2005, *ApJ*, **618**, L161
- Soummer, R., Pueyo, L., & Larkin, J. 2012, *ApJ*, **755**, L28
- Sparks, W. B., & Ford, H. C. 2002, *ApJ*, **578**, 543
- Stephens, D. C., Leggett, S. K., Cushing, M. C., et al. 2009, *ApJ*, **702**, 154
- Su, K. Y. L., Rieke, G. H., Stapelfeldt, K. R., et al. 2009, *ApJ*, **705**, 314
- Sudol, J. J., & Haghighipour, N. 2012, *ApJ*, **755**, 38
- Takata, M., Ouazzani, R. M., Saio, H., et al. 2020, *A&A*, **635**, A106
- Torres, C. A. O., Quast, G. R., Melo, C. H. F., & Sterzik, M. F. 2008, in *Young Nearby Loose Associations*, ed. B. Reipurth, 757
- Vigan, A., Moutou, C., Langlois, M., et al. 2010, *MNRAS*, **407**, 71
- Vigan, A., Gry, C., Salter, G., et al. 2015, *MNRAS*, **454**, 129
- Wahhaj, Z., Liu, M. C., Biller, B. A., et al. 2011, *ApJ*, **729**, 139
- Wahhaj, Z., Liu, M. C., Biller, B. A., et al. 2013, *ApJ*, **779**, 80
- Wahhaj, Z., Cieza, L. A., Mawet, D., et al. 2015, *A&A*, **581**, A24
- Wahhaj, Z., Milli, J., Kennedy, G., et al. 2016, *A&A*, **596**, L4
- Wang, J. J., Graham, J. R., Dawson, R., et al. 2018, *AJ*, **156**, 192
- Weinberger, A. J., Becklin, E. E., Schneider, G., et al. 1999, *ApJ*, **525**, L53
- Wilner, D. J., MacGregor, M. A., Andrews, S. M., et al. 2018, *ApJ*, **855**, 56
- Xuan, W. J., Mawet, D., Ngo, H., et al. 2018, *AJ*, **156**, 156
- Zuckerman, B., Rhee, J. H., Song, I., & Bessell, M. S. 2011, *ApJ*, **732**, 61
- Zurlo, A., Vigan, A., Mesa, D., et al. 2014, *A&A*, **572**, A85
- Zurlo, A., Vigan, A., Galicher, R., et al. 2016, *A&A*, **587**, A57